Optics Letters

Tunable mid-infrared source of light carrying orbital angular momentum in the femtosecond regime

Antoine Camper,[1,*] Hyunwook Park,[1] Yu Hang Lai,[1] Hiroyuki Kageyama,[2] Sha Li,[1] Bradford K. Talbert,[1] Cosmin I. Blaga,[1] Pierre Agostini,[1] Thierry Ruchon,[3] and Louis F. DiMauro[1]

[1]Department of Physics, the Ohio State University, Columbus, Ohio 43210, USA
[2]Department of Chemistry, School of Science, The University of Tokyo, 7-3-1 Hongo, Bunkyo-ku, Tokyo 113-0033, Japan
[3]LIDYL, CEA, CNRS, Université Paris-Saclay, CEA Saclay, 91191 Gif-sur-Yvette, France
*Corresponding author: camper.22@osu.edu

Received 11 August 2017; accepted 27 August 2017; posted 31 August 2017 (Doc. ID 304669); published 20 September 2017

We report on a tunable intense femtosecond mid-infrared (mid-IR) light source carrying orbital angular momentum (OAM). Our setup is based on an optical parametric amplification system with an 800 nm pump shaped with a spiral phase plate. We confirm the anisotropic OAM transfer from the pump to the idler through stimulated difference frequency generation by measuring the diffraction patterns of a triangular aperture illuminated by the signal, pump, and idler beams. The tunability of the setup is demonstrated by performing measurements at 3.0 and 3.6 μm idler wavelengths. This result provides a robust method of controlling OAM in strong field physics and designing secondary sources carrying OAM in the extreme ultraviolet spectral range through high-order harmonics generation.

OCIS codes: (140.3490) Lasers, distributed-feedback; (060.2420) Fibers, polarization-maintaining; (060.3735) Fiber Bragg gratings; (060.2370) Fiber optics sensors.

https://doi.org/10.1364/OL.42.003769

Light beams featuring helicoidal phase fronts have unique properties related to the orbital angular momentum (OAM) they carry [1], making them a one-of-a-kind subject for fundamental and applied investigations. Indeed, they are paradigms for general studies of lightwave singularities [2] and spin-orbit couplings [3]. On applicative standpoints, promising prospects for new forms of spectroscopies are envisioned with these beams, linked to the modifications of the usual transition selection rules [4]. They also offer an unbound observable, forming a basis for photon entanglement and optical communications only limited by the numerical aperture of the optical system [5]. They show exceptional imaging capacities of dislocations [6]. This list of prospects is representative of the majority of envisioned applications of beams with OAM, which is currently mostly limited to the static regime. However, implanting OAM into an intense ultrashort light beam opens a broad range of new possibilities such as time-resolved nonlocal spectroscopy in solids [7], magnetic sublevel resolved attosecond photoionization time-delay [8], multiphoton ionization [9], and molecular orientation [10]. It can also extend the generation of an OAM beam to the extreme ultraviolet range through high-harmonic generation (HHG) in gases [11–14], suited for investigations of direct one-photon photoionization processes in gases and solids. Despite these promising perspectives, OAM-related effects often remain elusive because the density of angular momentum along the direction of propagation is low. However, this quantity which is directly related to the amount of OAM per unit of linear momentum ℓ/k [1], where ℓ is the orbital angular momentum and k is the linear momentum, can be enhanced by increasing the OAM or the wavelength keeping the beam waist unchanged. As a result, long wavelengths can be used to enhance the sensitivity of OAM spectroscopy. In addition, since the ℓ/k ratio is conserved through HHG [12,13], this increase of sensitivity can be transferred to extreme ultraviolet (XUV)-OAM spectroscopy by using a mid-infrared (mid-IR) driver. This increase is expected to come along with the ability to generate XUV beams carrying OAM at higher photon energies compared to 800 nm at the same intensity [11–13], since the ponderomotive energy of strong field-driven electrons scales as the square of the wavelength, $\mathrm{Up} \propto \lambda^2$ [15].

So far, intense femtosecond beams with helicoidal phase fronts are only based on Ti:sapphire, which produces pulses with a central wavelength near 800 nm with limited tunability. Beam-shaping techniques originally developed for continuous-wave lasers were adapted to impart OAM on these ultrashort light pulses using, for instance, diffraction on a fork grating [16–19] and transmission through a spiral phase plate (SPP) [11,13,14,20–24]. However, intense femtosecond sources carrying OAM have not yet been demonstrated at longer wavelengths or with broad tunability. In particular, the simple SPP method cannot be directly transposed to this regime because of the lack of robust material. For example, two typical materials,

Si and Ge, are inadequate under exposure to high peak power mid-IR pulses because of their high nonlinear susceptibility. In this contribution, we report on an SPP-based scheme to generate tunable intense femtosecond mid-IR pulses carrying OAM that circumvents this problem. Our scheme is based on optical parametric amplification (OPA) pumped with+-SPP-shaped 800 nm femtosecond pulses. In contrast with spontaneous difference frequency generation (DFG) for which the OAM of the pump has equal probability to be transferred to the idler and the signal [25], we verify that in stimulated DFG the OAM of the pump is anisotropically transferred to the idler. We confirm this property of stimulated DFG for a pump with $\ell = 1$ and $\ell = -1$ by measuring the intensity profile of each pump, signal, and idler beams and characterizing their phase front properties by diffraction patterns of a triangular aperture. Finally, we demonstrate the tunability of our setup.

Our laser system consists of chirped pulse amplification at 800 nm, white light generation, and OPA stages. The 80 fs 800 nm pump with 12 mJ pulse energy is split into five arms. The first beam of 800 nm is used to generate white light in a sapphire plate, while the others drive OPA processes to produce the signal and idler beams. The signal wavelength can be tuned by adjusting the central wavelength of the seed and, as a result, the idler generated by stimulated DFG is tuned from 3 to 4 μm. In Fig. 1, the SPP is inserted in the 800 nm beam prior to the last OPA stage. We first place the SPP in the pump of the third OPA stage to prove the principle of the OAM transfer right after this stage, and then extend it to the 4th amplification stage for a high-energy option.

OAM anisotropic transfer in stimulated downconversion has been first demonstrated in the optical range with continuous-wave lasers [26]. More recently, it has been confirmed in the mid-IR with nanosecond pulses [27]. For beams with spiral phase fronts, OAM is associated with the helicity of the spiral. In nonlinear processes, the conservation of the phase front helicity is the consequence of the conservation of the wave vector imposed by phase-matching:

$$\mathbf{k}_p = \mathbf{k}_s + \mathbf{k}_i \rightarrow \ell_i = (\mathbf{r} \times \mathbf{k}_i) \cdot \mathbf{e}_z = (\mathbf{r} \times [\mathbf{k}_p - \mathbf{k}_s]) \cdot \mathbf{e}_z = \ell_p - \ell_s, \quad (1)$$

where the indices p, s, and i, respectively, stand for pump, signal and idler; $\mathbf{k}$ is the wavevector; ℓ is the helicity of the phase front associated with OAM; $\mathbf{r}$ is the vector position; and $\mathbf{e}_z$ is a unit vector along the direction of propagation. Since, in Eq. (1), any pair of integers (ℓ_s, ℓ_i) summing up to ℓ_p is a correct solution, it seems that (ℓ_s, ℓ_i) can take a set of different values. This actually turns out to be true in the case of spontaneous parametric down-conversion, as confirmed by the seminal work by Mair *et al.* [25], where the entanglement of the OAM state of signal and idler photons was first demonstrated. In this case, the OAM transfer is said to be isotropic. Later, OAM conservation in downconversion was confirmed in optical parametric oscillators (OPOs) [27,28] and in stimulated DFG [26,29]. In contrast with spontaneous DFG, the OAM transfer is anisotropic in these two cases. In the OPO case, the OAM is transferred to the signal: a mode-order-dependent Gouy phase shift in a half-symmetric cavity favors the buildup of the OAM mode in the signal over the idler. In the stimulated DFG case, the OAM is transferred to the idler: the OAM of the signal is imposed by the seed which keeps its characteristics throughout the amplification process. With this knowledge, two options are opened to generate an idler beam with $\ell_i = 1$ through stimulated DFG. One option is to generate the idler with the seed carrying the OAM and no OAM on the pump, in which case we expect $(\ell_s, \ell_i) = (-1, 1)$. To achieve spectral tunability, a set of SPPs designed for the different wavelengths or a broadband programmable deformable mirror to shape the seed is required. Alternatively, the pump beam for white light generation may carry an OAM, which would transfer directly to the seed [30] at the cost of potentially destructive self-focusing [31]. These two techniques limit the tunability of the setup. For this reason, we turn to the second option. It consists of generating the idler with the pump carrying the OAM and no OAM on the seed resulting in $(\ell_s, \ell_i) = (0, 1)$. This scheme is more favorable to get "turning knob" tunability. Indeed, it only requires a pump with OAM at a fixed wavelength in the last OPA stage, while the wavelength of the seed, which shows a standard flat wave front, is adjusted independently. For this reason, we choose to insert the SPP in the pump of the last OPA stage. Therefore, expect the OAM to be transferred from the pump to the idler, and the signal to carry $\ell_s = 0$, duplicating the properties of the seed.

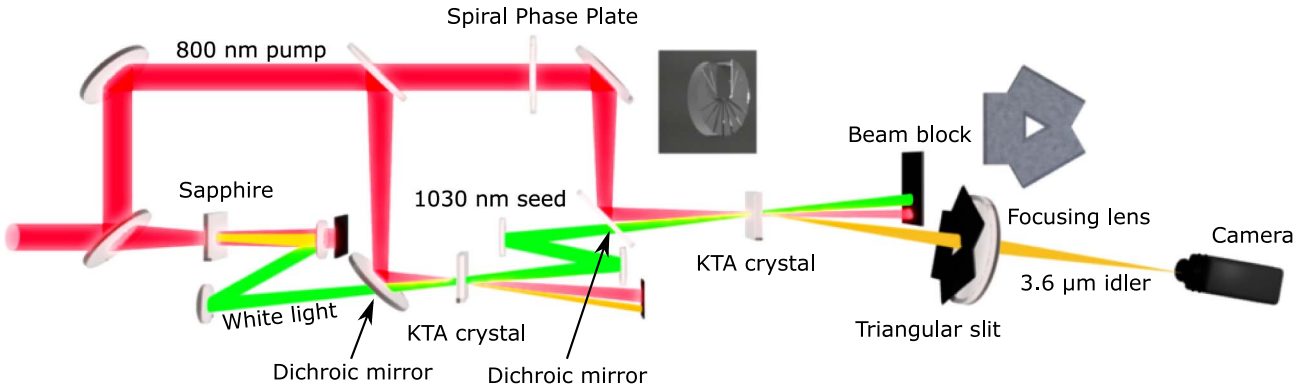

Fig. 1. OPA with OAM. A 16-level spiral phase plate (SILIOS Technologies) is placed in the 800 nm pump of the last OPA stage (the actual setup includes up to four OPA stages) yielding a 77.5% pure (1,0) Laguerre–Gaussian mode [20]. The 1030 nm seed with no OAM is amplified in a KTA crystal. The OAM is anisotropically transferred from the pump to the idler. A triangular aperture and a focusing lens are combined to characterize the helicity of the phase front of the pump, signal, and idler beams. The idler is imaged on an Electrophysics PV320 thermal camera. The pump and signal are imaged on a charge-coupled device camera.

The far-field images for a 3.6 μm idler beam obtained with and without the SPP in the pump beam are presented in Fig. 2. Without the SPP [Fig. 2(b)], the beam is a Gaussian mode. With the SPP in the pump [Fig. 2(d)], the idler beam profile presents a ring-like structure, with a minimum of intensity in its center. This intensity profile can be linked with either the phase singularity associated with the OAM of the idler or the intensity profile of the pump. Indeed, the DFG process is more efficient in the region of the pump where the intensity is the highest. In particular, although only the phase front of the pump is shaped, the propagation distance between the SPP and the OPA crystal is long enough for the intensity profile of the pump to present a minimum of intensity where the phase singularity is imprinted. As a result, the seed is amplified along the ring-like beam profile of the pump and the signal, as well as the idler, forms a donut shape at the exit of the OPA crystal. However, when propagated, the two beam profiles have very different properties. While the idler keeps its ring shape after propagation, as shown in Fig. 2(d), the signal does not. Based on the properties of Hankel transform, this is a strong indication that the OAM of the pump is anisotropically transferred from the pump to the idler and that the signal does not gain any OAM in the process.

To confirm these results, we measure the value of the OAM carried by each of the three beams involved in the DFG. Following the work by Hickmann *et al.* [32], we place an equilateral millimeter-size triangular slit in each beam after the OPA crystal. Immediately after this aperture, a 400 mm lens is used to reveal the diffraction pattern located at the focal plane of the lens. In Fig. 3, we illustrate the effects of an elliptical phase front with helicity ℓ on the diffraction pattern from a triangle slit. As reported in Ref. [32], the diffraction pattern is determined by the evolution of the phase, which contains the topological charge across each edge of the triangle slit. Indeed, a general property of diffraction is that a phase evolution $\phi(x)$ along a sharp edge is equivalent to add a $\nabla\phi$ wave vector to the diffracted beam. For a phase front with no helicity ($\ell = 0$) and a spherical phase front; the variations of the phase along each of the three edges of the triangle are even with respect to the middle of the edge. In this case, the diffraction pattern also has even symmetry and is not preferentially shifted in any particular direction in the Fourier plane. As illustrated in Fig. 2(e), the diffraction of a beam with a flat phase front shows a six-fold symmetry star-like pattern in which the most noticeable feature is an intense central spot. For a beam with a helicoidal phase front of helicity ℓ, the phase across each of the edges monotonically increases. As a result, the central spot observed for $\ell = 0$ in the Fourier plane is split into three spots, which are displaced from the optical axis. The shift is proportional to the slope of the phase variation in the direct space, and the direction is collinear to the orientation of the edge, in agreement with the addition of a $\nabla\phi$ wave vector to the diffracted beam. The symmetry of the diffraction pattern is reduced from six-fold to three-fold. Since the direction of the shift is determined by the slope of the phase across one edge of the triangle, this technique is sensitive to the magnitude and the sign of ℓ. In Figs. 2(g) and 2(i), we present numerical simulations based on Fraunhofer diffraction for $\ell = \pm 1$ and confirm the three-fold symmetry and the 180° rotation of the diffraction pattern when the sign of the OAM is flipped.

In the experiment, we first verify that the idler beam produced without SPP in the pump shows the expected six-fold symmetry, as shown in Fig. 2(f). We then place the SPP in the pump so that $\ell_p = 1$, and observe a threefold symmetry diffraction pattern [Fig. 2(h)] consistent with the simulation of $\ell_i = 1$ in Fig. 2(g). When the SPP is reversed in the pump to flip the sign of the topological charge, the diffraction pattern [Fig. 2(j)] is rotated by 180° as expected. This result also agrees with the simulation of $\ell_i = -1$ in Fig. 2(i). The imperfect contrast in the fringes of the diffraction pattern can be associated with an imperfect centering of the slit on the donut beam profile, a dependence of the phase front on the radial coordinate, and/or a residue of the $\ell_i = 0$ mode.

To confirm the tunability of our setup, we changed the seed wavelength to 1090 nm so that the idler wavelength is 3.0 μm, and repeat the measurement for $\ell_p = 1$ and $\ell_p = -1$. The results are presented in Fig. 4. The ring-like beam profile and its diffraction pattern through the triangle slit behave the same as for 3.6 μm. To establish the anisotropy of the OAM transfer, we also measure the diffraction patterns of the pump and the signal. As shown in Fig. 4, the diffraction patterns observed in the pump and idler beams are consistent with the two beams

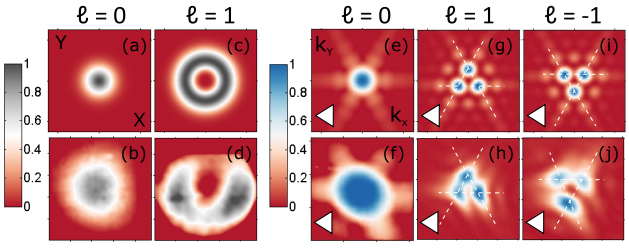

Fig. 2. Two rows represent the numerical simulation (top row) and the experimental results (bottom row) at 3.6 μm (the idler beam). From left to right: (a), (b) far-field intensity profiles of a Gaussian beam; (c), (d) a Laguerre–Gaussian with $\ell = 1$ and intensity profiles at the focus of a 400 mm focusing lens with a triangular aperture located right before the lens (the orientation of the aperture is represented on the bottom left corner of each inset) for incident laser beams with (e), (f) $\ell = 0$, (g), (h) $\ell = 1$, and (i), (j) $\ell = -1$. The intensity scales are arbitrary.

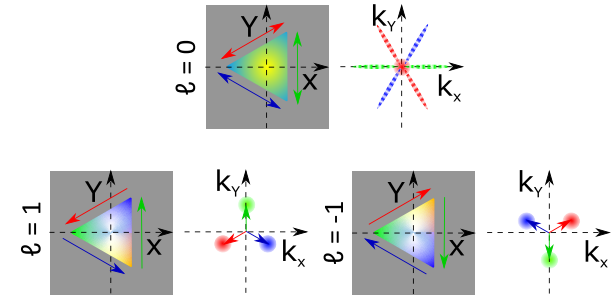

Fig. 3. OAM revealed by diffraction from a triangular aperture. (X, Y) is the direct space, and (k_X, k_Y) is the Fourier space (the focal plane of the lens). In the (X, Y) plane, the gray background is associated with no transmission; the colors are associated with phase variations. The arrows indicate the phase gradient $\nabla\phi$. The arrows in (k_X, k_Y) are color-matched with the ones in (X, Y) and indicate the associated shift of the diffraction pattern. For $\ell = 0$, the shifts are symmetry-forbidden. Each edge still provides diffraction in the orthogonal direction.

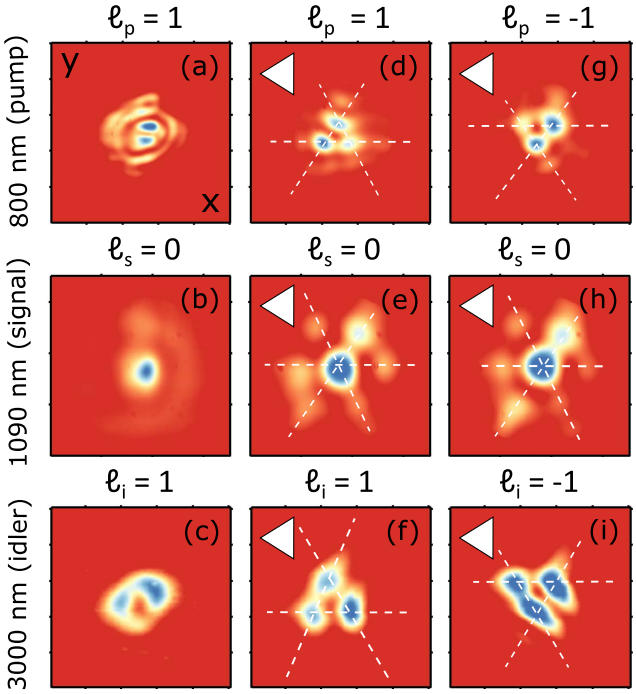

Fig. 4. OAM measurements from 0.8, 1.09, and 3.0 μm. From top to bottom: first, second, and third rows correspond to the 0.8, 1.09, and 3.0 μm beams, respectively. From left to right: the beam profiles at focus without the triangular slit, the diffraction patterns when $\ell_p = 1$, and the diffraction pattern of the triangular slit for $\ell_p = -1$. The orientation of the triangle is indicated in the top left corner of each inset.

carrying the same OAM, whereas the signal does not change, regardless of the sign of ℓ_p, maintaining the six fold symmetry of a topological charge $\ell_s = 0$. The measurements of the phase front helicity for each beam after the OPA stage verify the OAM anisotropic transfer from pump to idler.

The output pulse energy of the mid-IR beam with OAM is found to be 10 + μJ at the third amplification stage. To produce higher energy pulses, the SPP is inserted in the pump of the fourth amplification stage. We verify that the OAM is transferred to the idler without noticeable degradation of the beam quality by measuring the diffraction patterns. The output pulse energy reaches 250 μJ.

In conclusion, we have demonstrated the generation of hundreds of microjoule tunable mid-IR femtosecond pulses carrying OAM ±1. Our measurements confirm the anisotropic transfer of OAM from the pump to the idler in stimulated DFG. Our tunable setup opens new possibilities for tuning the OAM of XUV beams generated through HHG with mid-IR femtosecond pulses, as well as for OAM terahertz pulses generated through DFG.

Funding. Department of Energy (DOE), Office of Science (SC); Basic Energy Sciences (BES) (DE-FG02-04ER15614); National Science Foundation (NSF) (1605042); Air Force Office of Scientific Research (AFOSR) (FA9550-16-1-0013); Agence Nationale de la Recherche (ANR) (ANR-14-CE32-0010).

Acknowledgment. The authors thank Michel Bougeard for technical assistance.

REFERENCES

1. L. Allen, M. W. Beijersbergen, R. J. C. Spreeuw, and J. P. Woerdman, Phys. Rev. A **45**, 8185 (1992).
2. M. V. Berry, Proc. SPIE **3487**, 6 (1998).
3. K. Y. Bliokh, Y. Gorodetski, V. Kleiner, and E. Hasman, Phys. Rev. Lett. **101**, 030404 (2008).
4. M. van Veenendaal and I. McNulty, Phys. Rev. Lett. **98**, 157401 (2007).
5. G. Gibson, J. Courtial, M. J. Padgett, M. Vasnetsov, V. Pas'ko, S. M. Barnett, and S. Franke-Arnold, Opt. Express **12**, 5448 (2004).
6. Y. Yan, G. Xie, M. P. J. Lavery, H. Huang, N. Ahmed, C. Bao, Y. Ren, Y. Cao, L. Li, Z. Zhao, A. F. Molisch, M. Tur, M. J. Padgett, and A. E. Willner, Nat. Commun. **5**, 4876 (2014).
7. B. G. Mendis, Ultramicroscopy **157**, 1 (2015).
8. J. Wätzel and J. Berakdar, Phys. Rev. A **94**, 033414 (2016).
9. A. Afanasev, C. E. Carlson, and A. Mukherjee, Phys. Rev. A **88**, 033841 (2013).
10. P. K. Mondal, B. Deb, and S. Majumder, Phys. Rev. A **89**, 063418 (2014).
11. M. Zürch, C. Kern, P. Hansiger, A. Dreischuh, and C. Spielmann, Nat. Phys. **8**, 743 (2012).
12. G. Gariepy, J. Leach, K. T. Kim, T. J. Hammond, E. Frumker, R. W. Boyd, and P. B. Corkum, Phys. Rev. Lett. **113**, 153901 (2014).
13. R. Géneaux, A. Camper, T. Auguste, O. Gobert, J. Caillat, R. Taïeb, and T. Ruchon, Nat. Commun. **7**, 12583 (2016).
14. D. Gauthier, P. R. Ribič, G. Adhikary, A. Camper, C. Chappuis, R. Cucini, L. F. DiMauro, G. Dovillaire, F. Frassetto, R. Géneaux, P. Miotti, L. Poletto, B. Ressel, C. Spezzani, M. Stupar, T. Ruchon, and G. De Ninno, Nat. Commun. **8**, 14971 (2017).
15. P. Colosimo, G. Doumy, C. I. Blaga, J. Wheeler, C. Hauri, F. Catoire, J. Tate, R. Chirla, A. M. March, G. G. Paulus, H. G. Muller, P. Agostini, and L. F. DiMauro, Nat. Phys. **4**, 386 (2008).
16. I. G. Mariyenko, J. Strohaber, and C. J. G. J. Uiterwaal, Opt. Express **13**, 7599 (2005).
17. J. Strohaber, T. D. Scarborough, and C. J. G. J. Uiterwaal, Appl. Opt. **46**, 8583 (2007).
18. Y.-C. Lin, Y. Nabekawa, and K. Midorikawa, Appl. Phys. B **122**, 280 (2016).
19. A. Denoeud, L. Chopineau, A. Leblanc, and F. Quéré, Phys. Rev. Lett. **118**, 033902 (2017).
20. K. Sueda, G. Miyaji, N. Miyanaga, and M. Nakatsuka, Opt. Express **12**, 3548 (2004).
21. J. Strohaber, M. Zhi, A. V. Sokolov, A. A. Kolomenskii, G. G. Paulus, and H. A. Schuessler, Opt. Lett. **37**, 3411 (2012).
22. P. Hansinger, G. Maleshkov, I. L. Garanovich, D. V. Skryabin, D. N. Neshev, A. Dreischuh, and G. G. Paulus, Opt. Express **22**, 11079 (2014).
23. M. Miranda, M. Kotur, P. Rudawski, C. Guo, A. Harth, and A. L'Huillier, and C. L. Arnold, J. Mod. Opt. 1 (2016).
24. A. Leblanc, A. Denoeud, L. Chopineau, G. Mennerat, P. Martin, and F. Quéré, Nat. Phys. **13**, 440 (2017).
25. A. Mair, A. Vaziri, G. Weihs, and A. Zeilinger, Nature **412**, 313 (2001).
26. D. P. Caetano, M. P. Almeida, P. H. Souto Ribeiro, J. A. O. Huguenin, B. Coutinho dos Santos, and A. Z. Khoury, Phys. Rev. A **66**, 041801 (2002).
27. T. Yusufu, Y. Tokizane, M. Yamada, K. Miyamoto, and T. Omatsu, Opt. Express **20**, 23666 (2012).
28. A. Aadhi, G. K. Samanta, S. Chaitanya Kumar, and M. Ebrahim-Zadeh, Optica **4**, 349 (2017).
29. K. Furuki, M.-T. Horikawa, A. Ogawa, K. Miyamoto, and T. Omatsu, Opt. Express **22**, 26351 (2014).
30. H. I. Sztul, V. Kartazayev, and R. R. Alfano, Opt. Lett. **31**, 2725 (2006).
31. N. Neshev, A. Dreischuh, G. Maleshkov, M. Samoc, and Y. S. Kivshar, Opt. Express **18**, 18368 (2010).
32. J. M. Hickmann, E. J. S. Fonseca, W. C. Soares, and S. Chávez-Cerda, Phys. Rev. Lett. **105**, 053904 (2010).